Design and Stress Analysis of Bevel Line Gears with Vertical Flank Suitable for Micromachining

Yanjie Shao[1] – Yangzhi Chen[1,2,*] – Xiaoping Xiao[2] – Maoxi Zheng[1] – Weitao He[1]

[1] South China University of Technology, School of Mechanical and Automotive Engineering, China
[2] Guangdong Ocean University, School of Mechanical and Energy, China

The line gear (LG) exhibits promising applications in micromachinery owing to its simple structure and minimal teeth count. This paper aims to advance the meshing theory of LG and introduce a conical LG tooth configuration specifically tailored for micro-machining that is capable of driving with high performance. Based on the meshing principle of LG, a conical line gear pair with vertical flank (VFLG) of the driving gear was designed. Subsequently, adhering to the curvature non-interference principle that no local interference occurs in the meshing process and the specified range of fitting error in one direction, the design parameters for LG were determined. A comparison of the contact stress between two sets of different contact line types revealed the distinct advantage of VFLG with parameters identical to those of traditional LG. The experimental results conclusively demonstrate a transmission ratio error of 0.004, affirming the feasibility of the design. The curvature non-interference design formula proposed in this paper refines the LG design theory, and the novel LG design method presented holds significant implications for subsequent micromachining.
Keywords: line gear, bevel gear, meshing theory, stress analysis, micromachining

Highlights
- *A VFLG of a 2.5D structure was proposed, which is tailored for micromachining.*
- *Compared to the typical LG, the contact stress of the VFLG is significantly lower.*
- *LG's curvature non-interference theory was advanced, and its overall design theory was refined.*
- *The feasibility of the design was verified by kinematic experiments.*

0 INTRODUCTION

The growing demand for microsystems and miniaturized components has accelerated the need to manufacture high-quality microgears efficiently and economically [1] and [2]. Miniature gears are categorized based on their outer diameter range, with 0.1 mm to 10 mm considered the overall range, 1 mm to 10 mm termed as middle gears, and 0.1 mm to 1 mm classified as micro gears [3]. Notably, microgears have become key elements in a variety of microsystems owing to their ultra-lightweight, smaller size, and compactness [4]. The performance of the microsystem mainly depends on the quality of the microgear, and the overall quality of the gear depends on the manufacturing process. Among the commonly used processing technologies for microgears, additive processing stands out for its ability to fabricate complex components that are challenging to achieve through alternative methods [5]. However, a drawback is the tendency to generate pores during additive processing [6], leading to subpar mechanical properties. Additionally, the surface quality is constrained by the size of powder particles [7]. Electrical discharge machining (EDM) is known for its effectiveness and high precision, albeit with the drawback of low material removal rate and elevated equipment costs [8]. Furthermore, several widely employed micro-machining methods like micro-hobbing, micro-milling, and laser ablation are primarily tailored for machining spur gears, presenting limitations in processing traditional bevel gears [1] and [9]. Consequently, it is a viable approach to improve the geometric design of bevel gears to align with commonly used micro-machining methods [10].

In recent years, the emergence of new gear meshing theories has garnered significant attention. Tan et al. [11] introduced a novel tooth profile design method grounded in the conjugate curve theory, resulting in the development of the conjugate curve bevel gear. However, the normal section of the designed gear is convex with a convex arc, posing challenges for micro-machining. An et al. [12] presented the meshing theory of curve-pair bevel gears and designed a multi-point contact curve-pair bevel gear capable of achieving divisible axis intersection angles. Nevertheless, the tooth surface remains intricate and difficult to minimize. The line gear (LG) represents a novel gear mechanism rooted in spatial curve meshing theory [13]. Known for its characteristics, including that the minimum number of teeth can be 1 [14], flexible design, and controllable sliding rate [15], LG offers substantial advantages in

*Corr. Author's Address: South China University of Technology, School of Mechanical and Automotive Engineering, China, meyzchen@scut.edu.cn

483

terms of miniaturization and lightweight applications, such as vertical shaft reducer with transmission efficiency exceeding 99 %, lightweight parallel-axis LG reducer for sweeping robots, and non-trapped oil double-arc LG pumps [16] and [17]. Consequently, LG provides a feasible possibility for the miniaturization of conical gears. Currently, a conical LG with an outer diameter of 2.83 mm has been processed, and a transmission experiment has been conducted. However, the design principle and processing method impose limitations on further miniaturization; moreover, it suffers from the drawback of substantial contact stress [18].

While LG boasts a notable advantage in design flexibility, its design theory is not flawless. Chen et al. [19] derived the non-interference condition by testing the contact degree and kinematics. Chen et al. [13] proposed that it is crucial to ensure that there is no point on the driving wheel within the radius of the driving wheel tooth to avoid interference with the tooth surface during the LG parameter design process. However, the preceding discussion relies on kinematic geometric constraints in the design parameters, which alone cannot guarantee the correct mesh transmission of LG.

In this paper, based on the LG meshing theory, the meshing principle and tooth surface generation method for line gear with vertical flank (VFLG) are introduced. Characterized by a 2.5D structure, the gear is well-suited for micro-machining and allows for the accommodation of installation errors in a single direction. Moreover, the non-interference theory of LG curvature is proposed, contributing to the enhancement of LG's design theory. Also, a comparison of contact strength between VFLG and traditional LG is conducted. Ultimately, the accuracy of the design theory is validated through transmission tests.

1 THE MATHEMATICAL MODEL OF VFLG

1.1 The Meshing Theory of VFLG

The traditional LG meshing principle can be described as follows: the driving-driven contact line represents a pair of spatial conjugate curves designed by the active gear. This line consistently maintains tangential contact throughout the transmission process, with a shared principal normal at the tangent point. Each instantaneous contact point corresponds to a main normal plane for both the driving wheel and the driven wheel. The continuous surface formed by these curves constitutes the tooth surface of the driving and driven

gears. In contrast, the VFLG meshing theory adopts the point contact meshing between the vertical surface and the line. The vertical tooth face is 2.5D, making it more amenable to processing. Moreover, the "vertical surface-line" combination offers superior bearing capacity compared to the "line-line" configuration.

1.2 Coordinate System and Coordinate Transformation

As shown in Fig. 1. Meshing coordinate system of LG, in the space curved meshing coordinate system, the active contact line is fixed in coordinate system $S_1(o-x_1y_1z_1)$, and coordinate system S_1 rotates around coordinate system $S_o(o-xyz)$ with angular velocity ω_1, and the rotating angle is $\phi1$. The driven contact line is fixed in the coordinate system $S_2(o_2-x_2y_2z_2)$, and the coordinate system S_2 rotates around the coordinate system $S_p(o_p-x_py_pz_p)$ at the angular velocity ω_2, and the rotation angle is ϕ_2. a represents the distance from point o_p to the z axis, while b represents the distance from point o_p to the x-axis; θ represents the angle between the x-axis and x_p.
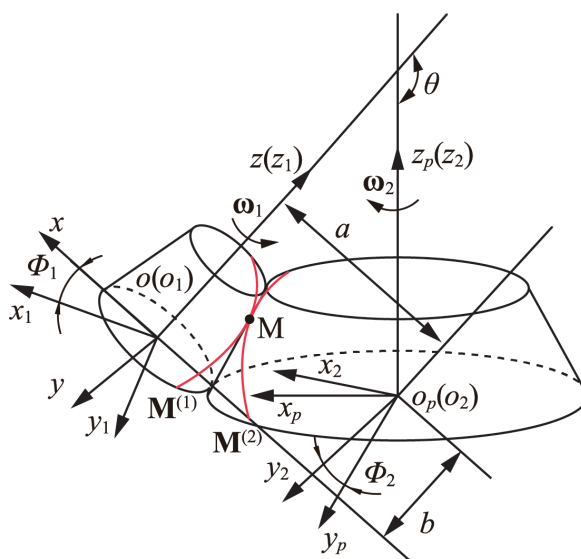

Fig. 1. *Meshing coordinate system of LG*

The coordinate transformation matrix between coordinate system $S_i(o_i-x_iy_iz_i)$ and coordinate system $S_j(o_j-x_jy_jz_j)$ is denoted as $\mathbf{M}_{ij}$. Here, three coordinate transformation matrices, $\mathbf{M}_{o1}$, $\mathbf{M}_{po}$ and $\mathbf{M}_{2p}$, are given, as shown in Eqs. (1) to (3) respectively.

$$\mathbf{M}_{o1} = \begin{bmatrix} \cos\phi_1 & \sin\phi_1 & 0 & 0 \\ -\sin\phi_1 & \cos\phi_1 & 0 & 0 \\ 0 & 0 & 1 & 0 \\ 0 & 0 & 0 & 1 \end{bmatrix}, \quad (1)$$

$$\mathbf{M}_{po} = \begin{bmatrix} -\cos\theta & 0 & -\sin\theta & b\sin\theta - a\cos\theta \\ 0 & 1 & 0 & 0 \\ \sin\theta & 0 & -\cos\theta & b\cos\theta + a\sin\theta \\ 0 & 0 & 0 & 1 \end{bmatrix}, \quad (2)$$

$$\mathbf{M}_{2p} = \begin{bmatrix} \cos\phi_2 & \sin\phi_2 & 0 & 0 \\ -\sin\phi_2 & \cos\phi_2 & 0 & 0 \\ 0 & 0 & 1 & 0 \\ 0 & 0 & 0 & 1 \end{bmatrix}. \quad (3)$$

The transformation matrix between coordinate system S_1 and coordinate system S_2 can be obtained, as shown in Eq. (4).

$$\mathbf{M}_{21} = \mathbf{M}_{2p} \cdot \mathbf{M}_{po} \cdot \mathbf{M}_{o1}. \quad (4)$$

1.3 Meshing Equation

The relative speed of the main and slave driving wheel at the engagement point is expressed in Eq. (5).

$$\mathbf{v}_{12} = \begin{pmatrix} y_1^{(o)}(\omega_1 - \omega_2\cos\theta) \\ \\ -x_1^{(o)}\omega_1 + (a + x_1^{(o)})\omega_2\cos\theta \\ -(b - z_1^{(o)})\omega_2\sin\theta \\ \\ -y_1^{(o)}\omega_2\sin\theta \end{pmatrix}, \quad (5)$$

where, $x_1^{(o)}, y_1^{(o)}, z_1^{(o)}$ can be obtained by $x_1^{(1)}, y_1^{(1)}, z_1^{(1)}$ through $\mathbf{M}_{o1}$.

The meshing equation is denoted in Eq. (6).

$$\mathbf{v}_{12} \cdot \boldsymbol{\beta} = \mathbf{0}, \quad (6)$$

where β represents the principal normal vector of the driving contact line at the meshing point.

$\phi_1 = t$ can be deduced by substituting the relative velocity in Eq. (7).

1.4 Contact Curve and Centre Curve

In the coordinate system S_1, the position vector of the active contact line is shown as Eq. (7).

$$\mathbf{r}_1^{(1)} = (mg(t)\cos t, \ mg(t)\sin t, \ ng(t), \ 1) \quad (7)$$

And $\mathbf{r}_{1-3D}^{(1)}$ is shown in Eq. (8).

$$\mathbf{r}_{1-3D}^{(1)} = (mg(t)\cos t, \ mg(t)\sin t, \ ng(t)). \quad (8)$$

The equations for the driving contact curve are given in Eq. (9).

$$\mathbf{M}^{(1)} = \begin{cases} x_1 = mg(t)\cos t \\ y_1 = mg(t)\sin t, \\ z_1 = ng(t) \end{cases} \quad (9)$$

where $n = i_{12}m$, and the driven contact curve can be obtained in Eq. (10).

$$\mathbf{M}^{(2)} = \begin{cases} x_2 = -(m\cos\theta + n\sin\theta)\cdot g(t)\cos(t/i_{12}) \\ y_1 = (m\cos\theta + n\sin\theta)\cdot g(t)\sin(t/i_{12}) \\ z_1 = (-n\cos\theta + m\sin\theta)g(t) \end{cases} \quad (10)$$

As depicted in Fig. 2. Diagram of VFLG's normal vector, in contrast to the conventional LG, the normal vector can be directly obtained from $\mathbf{M}^{(1)}$ and represents the normal vector projected onto the bottom surface of the active contact line, as illustrated in Eq. (11)

$$\mathbf{n}^{(1)} = [-\sin t, \cos t, 0]^{\mathrm{T}}. \quad (11)$$

The equations for the driven centring curve are expressed in Eq. (12)

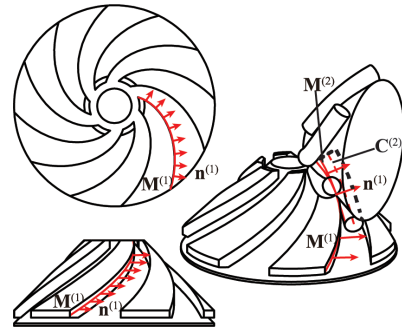$$\mathbf{C}_2^{(2)} = \mathbf{r}_{2-3D}^{(2)} \pm l_2 \cdot \mathbf{n}^{(2)}/2. \quad (12)$$

Fig. 2. *Diagram of VFLG's normal vector*

1.5 Geometrical Modelling

The conventional LG tooth surface construction method is illustrated in Fig. 3. Construction method of driven LG tooth surface. Following the determination of the cross-section profile, a scanning method is employed for modelling [18]. In this approach, the contact curve serves as the scan line; the centre line acts as the guideline.

The modelling method of VFLG is simpler, as depicted in Fig. 4. Construction method of driving VFLG tooth surface. Initially, the plane contour is determined, followed by a combination of stretching and rotary cutting.
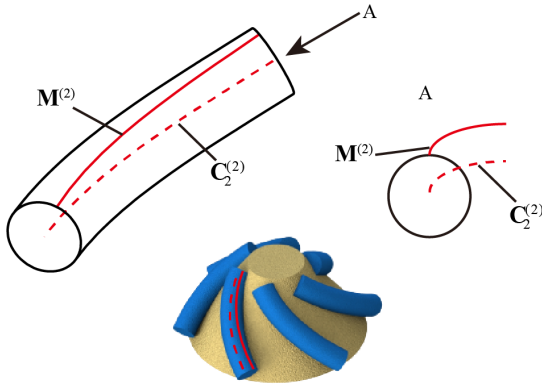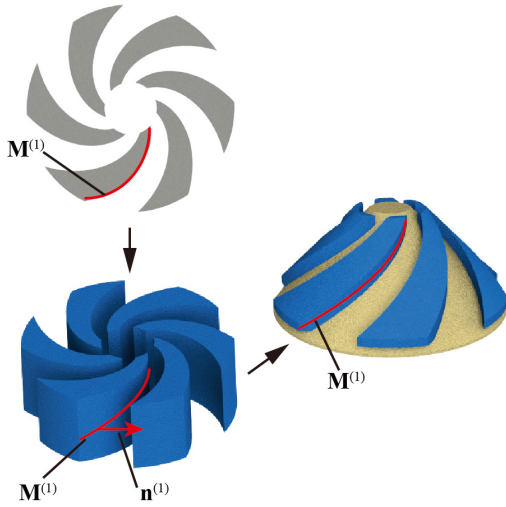
Fig. 3. *Construction method of driven LG tooth surface*

Fig. 4. *Construction method of driving VFLG tooth surface*

2 CORRECT MESHING CONDITIONS CONSIDERING CURVATURE INTERFERENCE AND MISALIGNMENT

2.1 Curvature Non-Interference Conditions

Illustrated in Fig. 5. Diagram of tangent plane and common normal, the two surfaces are tangent at point M, with **n** representing the common normal line. Assuming that the n direction corresponds to the spatial direction of the driving wheel teeth, the curvature does not interfere, and the induced curvature k_{b1} should satisfy the condition $k_{b1} \geq 0$ in any direction.

The induced curvature in any direction can be obtained by Euler's formula, as shown in Eq. (13).

$$k_{b1} = k_1 \cos^2(\varphi + \Delta) + k_2 \sin^2(\varphi + \Delta). \quad (13)$$

As shown in Fig. 6, where $\tan 2\varphi = 2\tau_{a1}/(k_{a2}-k_{a1})$, k_1 and k_2 are the principal curvature of the surface and $k_1 > k_2$, τ_{a1} is the tangential induced torsion.
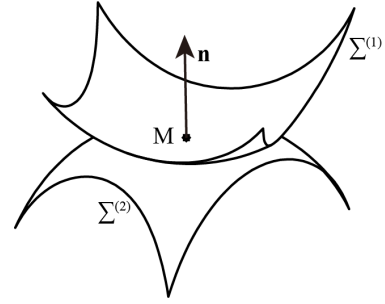

Fig. 5. *Diagram of tangent plane and common normal*
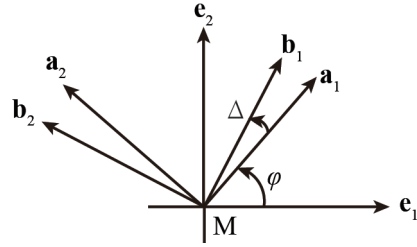

Fig. 6. *The relationship between k_n and τ_n in all directions on a surface*

Here, k_{b1} can also be expressed as Eq. (14).

$$k_{b1} = k_{a1} \cos^2 \Delta + 2\tau_{a1} \sin \Delta \cos \Delta + k_{a2} \sin^2 \Delta. \quad (14)$$

According to Section 2.1, Eq. (14) must be a non-negative definite quadratic function, then $(2\tau_{a1})^2 - 4 k_{a1}k_{a2} \leq 0$. Therefore, the curvature non-interference condition of LG can be summarized as Eq. (15).

$$\begin{cases} k_{a1}, k_{a2} \geq 0 \\ k_{a1}k_{a2} \geq \tau_{a1}^2 \end{cases}. \quad (15)$$

The pair of tangential and normal induced curvature, perpendicular to each other, can be incorporated into the calculation. In the above formula, k_{a1} is defined as the tangential induced curvature, k_{a2} is defined as the normal induced curvature, and τ_{a1} is the tangential induced geodesic torsion, which are solved below.

2.2 Requirements for Value of Parameters

2.2.1 Tangential Induced Curvature

The normal curvatures of curves $\mathbf{M}^{(1)}$ and $\mathbf{M}^{(2)}$ are shown in Eqs. (16) (17) respectively.

$$k_1^1 = \left| \mathbf{r}_1^{1(1)} \times \mathbf{r}_1^{1(2)} \right| / \left| \mathbf{r}_1^{1(1)} \right|^3, \quad (16)$$

$$k_1^2 = \left| \mathbf{r}_1^{2(1)} \times \mathbf{r}_1^{2(2)} \right| / \left| \mathbf{r}_1^{2(1)} \right|^3. \quad (17)$$

From Meusnier's theorem, the induced curvature of the tangent can be obtained as Eq. (18).

$$k_{a1} = k_1^1 \cos\varphi_1 - k_1^2 \cos\varphi_2, \qquad (18)$$

where φ_1(turning angle), φ_2 are the angles of $\boldsymbol{\beta}_1$ and $\boldsymbol{\beta}_2$ respectively with $\mathbf{n}$, as shown in 2.2.2 Normal Induced Curvature.
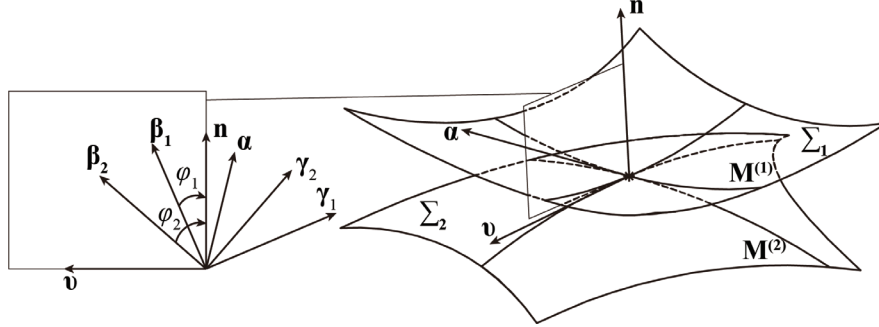

Fig. 7. *Diagram of the turning angle of LG*

2.2.2 Normal Induced Curvature

As shown in Fig. 8, the normal induced curvature can be indicated in Eq. (19)

$$k_{a2} = 1/R_1 + 1/R_2 = 2/l_1 + 2/l_2, \qquad (19)$$

where, R_1, R_2, l_1, l_2 are respectively the radius of curvature and the diameter of curvature at the meshing point.
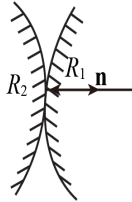

Fig. 8. *Schematic diagram of normal surface curvature radius*

2.2.3 Tangentially Induced Geodesic Torsion

The geodesic torsion of $\mathbf{M}^{(1)}$ to $\sum_1$ and $\mathbf{M}^{(2)}$ to $\sum_2$ are denoted in Eqs. (20) d (21) respectively.

$$\tau_{g1} = \tau_1 + \dot{\varphi}_1 = \tau_1 + d\varphi_1/ds_1, \qquad (20)$$

$$\tau_{g2} = \tau_2 + \dot{\varphi}_2 = \tau_2 + d\varphi_2/d\varphi_2, \qquad (21)$$

where $\tau_1 = (\mathbf{r}_1^{1(1)} \times \mathbf{r}_1^{1(2)}) \cdot \mathbf{r}_1^{1(3)}/\left|\mathbf{r}_1^{1(1)} \times \mathbf{r}_1^{1(2)}\right|$ and

$\tau_2 = (\mathbf{r}_2^{2(1)} \times \mathbf{r}_2^{2(2)}) \cdot \mathbf{r}_2^{2(3)}/\left|\mathbf{r}_2^{2(1)} \times \mathbf{r}_2^{2(2)}\right|$.

Finally, the tangential-induced geodesic torsion is expressed as Eq. (22).

$$\tau_{a1} = \tau_{g1} - \tau_{g2}. \qquad (22)$$

Hence, the curvature non-interference condition of LG can be translated into Eq. (23), allowing for the derivation of the value requirements for relevant parameters in the modelling of VFLG.

$$\begin{cases} \dfrac{\left|\mathbf{r}_1^{1(1)} \times \mathbf{r}_1^{1(2)}\right|}{\left|\mathbf{r}_1^{1(1)}\right|^3} \cos\varphi_1 - \dfrac{\left|\mathbf{r}_1^{2(1)} \times \mathbf{r}_1^{2(2)}\right|}{\left|\mathbf{r}_1^{2(1)}\right|^3} \cos\varphi_2 \geq 0 \\[2ex] \left(\dfrac{\left|\mathbf{r}_1^{1(1)} \times \mathbf{r}_1^{1(2)}\right|}{\left|\mathbf{r}_1^{1(1)}\right|^3} \cos\varphi_1 - \dfrac{\left|\mathbf{r}_1^{2(1)} \times \mathbf{r}_1^{2(2)}\right|}{\left|\mathbf{r}_1^{2(1)}\right|^3} \cos\varphi_2\right)\left(\dfrac{2}{l_1} + \dfrac{2}{l_2}\right) \geq \tau_{a1}^2 \\[2ex] \tau_{a1} = \dfrac{(\mathbf{r}_1^{1(1)} \times \mathbf{r}_1^{1(2)}) \cdot \mathbf{r}_1^{1(3)}}{\left|\mathbf{r}_1^{1(1)} \times \mathbf{r}_1^{1(2)}\right|} - \dfrac{(\mathbf{r}_2^{2(1)} \times \mathbf{r}_2^{2(2)}) \cdot \mathbf{r}_2^{2(3)}}{\left|\mathbf{r}_2^{2(1)} \times \mathbf{r}_2^{2(2)}\right|} + \dfrac{d\varphi_1}{ds_1} - \dfrac{d\varphi_2}{ds_2} \end{cases} (23)$$

2.3 Misalignment Adaptability for One Direction

If there is a certain installation error in the direction of the driving wheel axis. Assume that the installation parameter b is in one direction in Fig. 9 has an installation error δb. The equations for the driven contact curve are donated as $\mathbf{M}^{(2)}$ in Eq. (10), and $\mathbf{M}_{\delta b}^{(1)}$ can be expressed as Eq. (24)

$$\mathbf{M}_{\delta b}^{(1)} = \begin{cases} mg(t)\cos t \\ mg(t)\sin t \\ ng(t) - \delta b \end{cases}. \qquad (24)$$

It can be observed that, in comparison with $\mathbf{M}^{(1)}$ and $\mathbf{M}_{\delta b}^{(1)}$, there is only a deviation in the Z-axis direction, as illustrated in Fig. 10. The offset contact line remains on the tooth surface of the driving wheel. Consequently, VFLG exhibits adaptability to installation errors in one direction. Theoretically, its allowable error range is h_1 (the height of the vertical

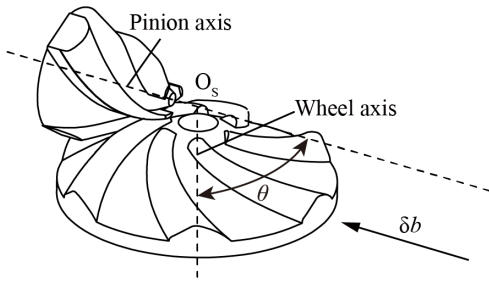plane), and specific values can be determined based on the required error range.

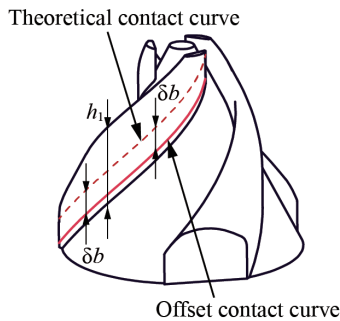**Fig. 9.** *Assembly error diagram of VFLG*

Fig. 10. *Assembly error adaptability of VFLG*

3 STRESS ANALYSIS AND COMPARISON WITH CONVENTIONAL LG

To compare the load-carrying capacity of VFLG and LG ($\varphi_1 = \pi/6$) [18], a finite element model was utilized to analyse the load stress on both gear types. Since many analyses have been done in previous research, two sets of different types of contact lines were used here for analysis and comparison. The material selected was stainless steel, featuring a Young's modulus of 2e5 MPa and a Poisson's ratio of 0.3. In Section 4.1, the maximum outside diameter of the

driving wheel was 3.2 mm, the maximum size of the triangular unit on the tooth surface was 2e–5 mm, the applied torque was increased to 5e–3 Nmm from 0 Nmm, and the rotational speed was kept at 10 r/min. In Section 4.2, the maximum outer diameter of the driving wheel was 11 mm, the maximum size of the unit was 2e–4 mm, the applied torque was increased to 5e–2 Nmm from 0 Nmm, and the rotational speed was kept at 10 r/min. The speed and torque settings are depicted in Fig. 11, and two pairs of rigid surfaces were built to apply rotation velocity and torque (Fig. 11).
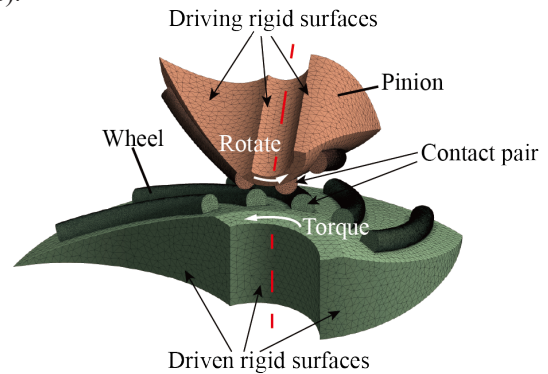

Fig. 11. *Schematic of finite element model*

3.1 Equidistant Spiral Bevel Gear

The equations for the driving contact curve are given as Eq. (25).

$$M^{(1)} = \begin{cases} x_1 = g(t)\cos t \\ y_1 = g(t)\sin t \\ z_1 = 2g(t) \end{cases}. \tag{25}$$

For LG and VFLG, $g(t)$ is t and e^t, respectively, and the results obtained after substituting the curvature calculation condition Eq. (23) are deduced as Eqs. (26) and (27) respectively.

$$\frac{2}{l_1} + \frac{2}{l_2} \geq \frac{\left(5+t^2\right)^{3/2}\left(2400+940t^2+124t^4+5t^6\right)^2}{\sqrt{3}\left(20+8t^2+t^4\right)^2\left(80+17t^2+t^4\right)^2\left(2\sqrt{20+8t^2+t^4}-\sqrt{80+17t^2+t^4}\right)}, \tag{26}$$

$$\begin{cases} \dfrac{2}{l_1} + \dfrac{2}{l_2} \geq \dfrac{81\left(4t^2+17\right)^{3/2}\sqrt{t^4+20t^2+68}\,/\,2\,/\,t}{p(t)+q(t)} \\ p(t) = \left(t^2+34\right)\left(4t^2+17\right)^{3/2}\sqrt{t^4+20t^2+68} \\ q(t) = \sqrt{16t^4+88t^2+153}\left(t^2+17\right)^{3/2}\left(t\left(t^2+18\right)\sin\left(\dfrac{3t}{2}\right)-\left(t^2+34\right)\cos\left(\dfrac{3t}{2}\right)\right) \end{cases}. \tag{27}$$

Here, while solving for the curvature diameter at the meshing point of VFLG, as illustrated in Fig. 12. Outline of VFLG tooth surface in normal section, the yellow normal phase contour is acquired, and subsequently, the curvature at the meshing point is determined through approximate fitting.

To facilitate the comparison of contact stress, it is imperative to ensure that curvature interference does not occur under the same parameters. The parameters chosen through the integrated formula Eqs. (26) and (27) are defined as Eq. (28), with w_1 representing the width of VFLG gear teeth.

$$\begin{cases} \pi / 3 \le t \le \pi / 3 + 11\pi / 40 \\ l_1 = l_2 = w_1 = 0.3 \text{ mm} \end{cases}. \tag{28}$$
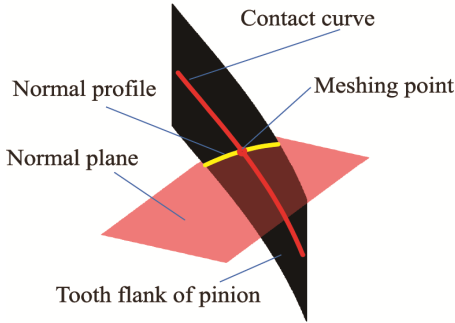

Fig. 12. *Outline of VFLG tooth surface in normal section*

Table 1. *Modelling parameters of equidistant spiral LG and VFLG*

Parameters	m [mm]	n [mm]	l_1/w_1 [mm]	l_2 [mm]	a,b [mm]	i_{12}	θ	$g(t)$
LG	1	2	$l_1=0.3$	0.3	0,0	2	$\pi/2$	t
VFLG	1	2	$w_1=0.3$	0.3	0,0	2	$\pi/2$	t

The VFLG and LG gear pairs were established using the parameters listed in Table 1. Modelling parameters of equidistant spiral LG and VFLG are depicted in Figs. 13a and b, respectively. A comparison of maximum stress changes between the two is illustrated in Fig. 14.
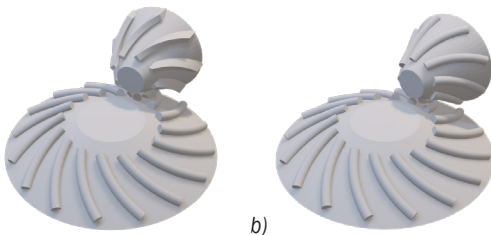

Fig. 13. *The model diagram used in finite element simulation: a) VFLG; b) LG*
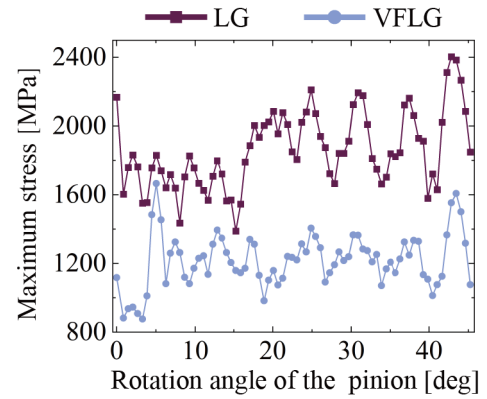

Fig. 14. *Comparison diagram of maximum contact stress on tooth surfaces of equidistant helix LG and VFLG*

3.2 Equiangular Spiral Bevel Gear

Similarly, the calculation results for LG and VFLG curvature non-interference are depicted in Eqs. (29) and (30), respectively.

$$2 / l_1 + 2 / l_2 \ge \frac{25\mathrm{e}^{-t}}{12\sqrt{2} - 6\sqrt{5}}, \tag{29}$$

$$\frac{2}{l_1} + \frac{2}{l_2} \ge -\frac{63\mathrm{e}^{-2t}}{4(-7 + 3\sqrt{10}\cos\frac{3t}{2} - 3\sqrt{10}\sin\frac{3t}{2})}. \tag{30}$$

The range of parameters selected is expressed in Eq. (31).

$$\begin{cases} \pi / 4 \le t \le \pi / 4 + 11\pi / 40 \\ l_1 = w_1 = 0.6 \text{ mm}, l_2 = 0.8 \text{ mm} \end{cases}. \tag{31}$$

The comparison of maximum stress changes between LG and VFLG is shown in Fig. 15, and parameters used for modelling are listed in Table 2.
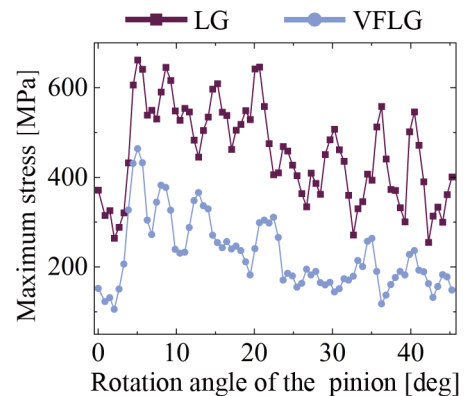

Fig. 15. *Comparison diagram of maximum contact stress on tooth surfaces of equiangular helix LG and VFLG*

Table 2. *Modelling parameters of equiangular spiral LG and VFLG*

Parameters	m [mm]	n [mm]	l_1/w_1 [mm]	l_2 [mm]	a,b [mm]	i_{12}	θ	$g(t)$
LG	1	2	$l_1=0.6$	0.8	0,0	2	$\pi/2$	e^t
VFLG	1	2	$w_1=0.6$	0.8	0,0	2	$\pi/2$	e^t

3.3 Contact Stress Analysis

As depicted in Fig. 14, in Section 4.1, the contact stress is relatively large when the single-tooth meshing is about to end. This phenomenon arises from the transition from single-tooth load to two teeth at approximately 43°. The contact between the driving and driven contact line teeth at the top of the tooth causes stress concentration, leading to an increase in contact stress.

In Section 4.2 (Fig. 15) and Section 4.1 for VFLG, the position of the maximum contact stress is around 5°. This is attributed to the transformation of the two-tooth transmission into a single-tooth transmission, where the load is not shared, consequently amplifying the contact stress.

From Figs. 14 and 15, it is evident that the average contact stress of VFLG is nearly half that of LG, irrespective of whether the contact line is an equidistant helix or an equiangular helix. Without parameter optimization, when the active contact line is an isometric helix, the maximum contact stress of LG, modelled by the optimal contact stress method in [18], is 2404.1 MPa, whereas that of VFLG is 1665.5 MPa. Similarly, when it is an equiangular helix, the maximum contact stress is 662.2 MPa for LG and 463.9 MPa for VFLG, respectively. During the single tooth meshing period in Section 4.2, both the finite element analysis results, as shown in Fig. 16, indicate that the approximate contact ellipse long axis and short axis for LG are 34.01 μm and 7.93 μm, respectively, while those for VFLG are 39.2 μm and 9.58 μm. According to [20], the size of the contact stress is inversely proportional to the product of the major semi-axis and the short semi-axis of the contact ellipse. Clearly, the contact ellipse of VFLG is larger and exhibits better bearing capacity.

The meshing principle of VFLG is improved to vertical bearing on the basis of LG. During the transmission process, the contact stress is optimized by increasing the contact ellipse. The results of finite element analysis indicate that VFLG exhibits a significant advantage in bearing capacity.

4 TRANSMISSION EXPERIMENT

The designed driving wheel is a microgear with a diameter of 0.9 mm. It was manufactured using a stereo lithography apparatus (SLA) after being enlarged 20 times in equal proportion. The speed of the driving and driven wheels was collected by torque sensors, and the instantaneous transmission ratio can be calculated based on the collected speed data. The parameters used are listed in Table 3. In the experiment, the power of the driving gear was transmitted by a servomotor at a speed of 300 r/min, and the load was provided by a magnetic damper at 20 Nmm. Subsequently, a transmission experiment was conducted, and the actual manufactured VFLG sample aligns with the theoretical model in Fig. 17. The transmission ratio test was performed on the VFLG kinematics test facility depicted in Fig. 18, and the results are shown in Fig. 19.

As evident from Fig. 19, the instantaneous transmission ratio of the gear pairs in the processed sample line fluctuates around 2, with an average value of 2.004 and a standard deviation of 0.003. In the actual transmission process, the elastic deformation of the gear and the load sharing of the contact teeth will affect the transmission ratio [21]. In this study, the influence of elastic deformation on the transmission ratio is dominant as the material used is photosensitive resin. Specifically, as shown in Fig. 20, when the
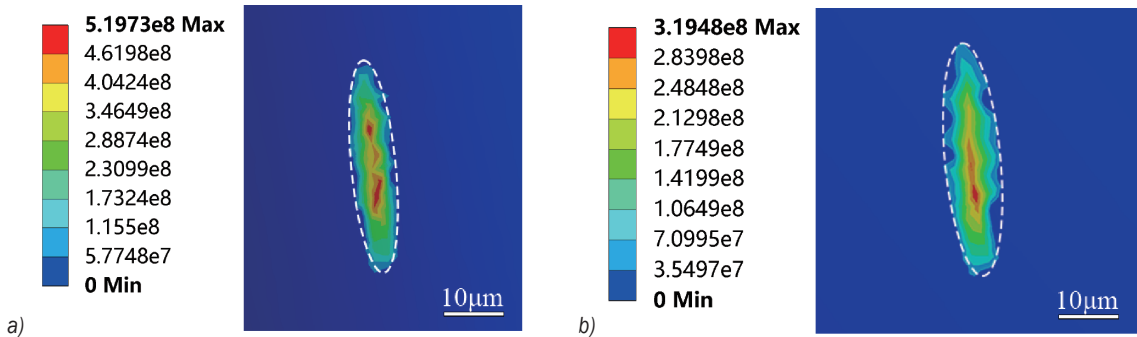

a)

b)

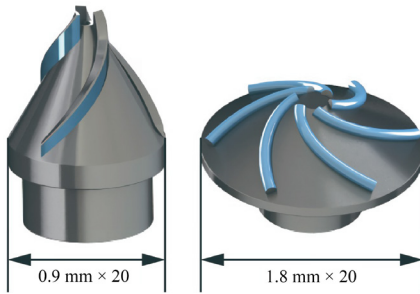**Fig. 16.** *Finite element analysis results of LG and VFLG; a) LG; b) VFLG*

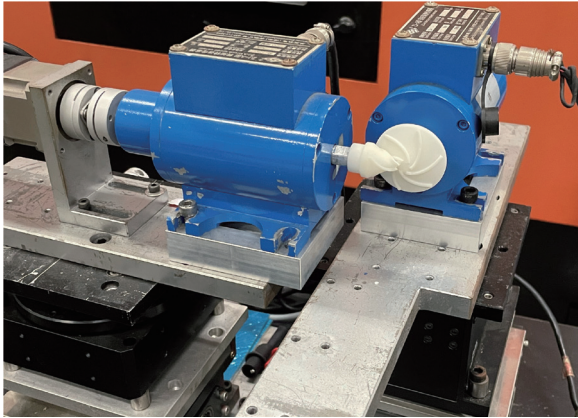**Fig. 17.** *Vertical gear pair used in the experiment*

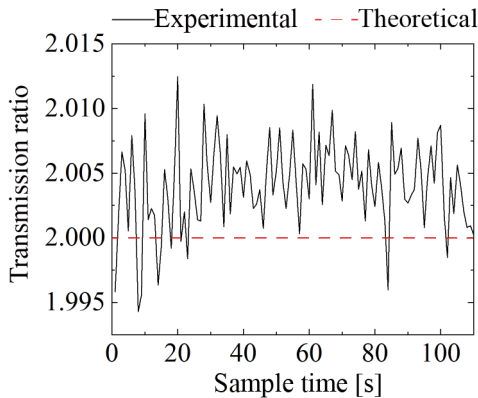**Fig. 18.** *Schematic diagram of experimental apparatus*

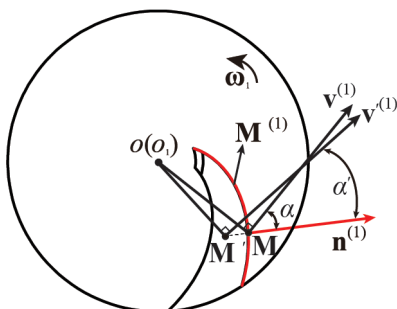**Fig. 19.** *Schematic diagram of kinematic experiment results*

Fig. 20. *Schematic diagram of instantaneous pressure angle variation at the point of meshing*

load increases, the elastic deformation causes the actual point of engagement to shift from M point to M' point, and the corresponding theoretical and actual instantaneous pressure angles are denoted as α and α', respectively. Obviously, the influence of the load causes the pressure angle to decrease. It is worth noting that the pressure angle has a significant effect on the transmission ratio [22] and [23]. As the pressure angle decreases, the torque capacity of the driving wheel increases [24], thus increasing the linear speed of the driven wheel; at the same time, manufacturing errors and installation errors also have a certain impact, ultimately resulting in a slightly higher transmission ratio than the theoretical value. Nevertheless, it demonstrates that the meshing principle and vertical tooth configuration proposed in this paper are feasible.

Table 3. *Parameters of VFLG used for the experiment*

Parameters	m [mm]	n [mm]	l_1/w_1 [mm]	l_2 [mm]	a,b [mm]	i_{12}	θ	$g(t)$
VFLG	0.5	1	$w_1=0.2$	0.1	0,0	2	$\pi/2$	$t/5$

5 CONCLUSIONS

Previous work on LG primarily focused on contact analysis, slide rate, centre distance separability of parallel-axis gears, etc. However, there is a lack of further research on the feasibility of generating tooth surfaces, and a deficiency in simple and feasible LG tooth configuration design in the field of micro and nano drives.

In this paper, the mathematical model of the vertical gear pair is described, emphasizing the advantages of the new gear pair in terms of load capacity and machining difficulty through analysis. Building upon this foundation, the design criteria of the gear pair are improved, and the conditions of non-interference of the curvature of the LG are deduced. Finally, a pair of special gears is designed and manufactured, validating the feasibility of the design of the VFLG.

The conclusion of this paper is as follows:
1. The VFLG features a 2.5D tooth configuration, offering the advantages of low difficulty and easy accuracy guarantee in the machining of micro-gears. In theory, it can adapt to commonly used micro-machining methods such as micro-milling and laser ablation.
2. The curvature non-interference formula of LG is derived, restricting the value of the turning angle

and the curvature radius at the meshing point of the normal plane.

3. The maximum contact stress of VFLG is lower than that of traditional LG, indicating better bearing capacity. This feature positions VFLG as a promising candidate for applications in the micro and nano fields.

These findings have propelled the development of LG in the field of micro and nano applications. However, this paper solely designed an LG suitable for micro-machining and feasible in principle; the micromachining has not been carried out, and the actual tribological performance, transmission capacity and transmission efficiency of VFLG are uncertain. Future work will involve utilizing the new gear pair for micro-machining objects, such as laser ablation, to assess its accuracy level. Additionally, micro-transmission experiments will be conducted to study transmission accuracy and explore its applications in the field of MEMS, such as micro pumps and micro robots.

6 ACKNOWLEDGEMENTS

7 REFERENCES

[1] Jain, N.K., Chaubey, S.K. (2017). 1.17 Review of Miniature Gear Manufacturing. Hashmi, M.S.J. (ed.) *Comprehensive Materials Finishing*, p. 504-538, Elsevier, **DOI:10.1016/B978-0-12-803581-8.09159-1**.

[2] Chaubey, S.K., Jain, N.K. (2018). State-of-art review of past research on manufacturing of meso and micro cylindrical gears. *Precision Engineering*, vol. 51, p. 702-728, **DOI:10.1016/j.precisioneng.2017.07.014**.

[3] Chaubey, S.K., Jain, N.K. (2019). Analysis and multi-response optimization of gear quality and surface finish of meso-sized helical and bevel gears manufactured by the WSEM process. *Precision Engineering*, vol. 55, p. 293-309, **DOI:10.1016/j.precisioneng.2018.09.019**.

[4] Wang, Y., Chen, X., Wang, Z., Dong, S. (2018). Fabrication of micro gear with intact tooth profile by micro wire electrical discharge machining. *Journal of Materials Processing Technology*, vol. 252, p. 137-147, **DOI:10.1016/j.jmatprotec.2017.09.002**.

[5] Rejeski, D., Zhao, F., Huang, Y. (2018). Research needs and recommendations on environmental implications of additive manufacturing. *Additive Manufacturing*, vol. 19, p. 21-28, **DOI:10.1016/j.addma.2017.10.019**.

[6] Reijonen, J., Revuelta, A., Riipinen, T., Ruusuvuori, K., Puukko, P. (2020). On the effect of shielding gas flow on porosity and melt pool geometry in laser powder bed fusion additive manufacturing. *Additive Manufacturing*, vol. 32, 101030, **DOI:10.1016/j.addma.2019.101030**.

[7] Opatová, K., Zetková, I., Kučerová, L. (2020). Relationship between the size and inner structure of particles of virgin and re-used MS1 maraging steel powder for additive manufacturing. *Materials*, vol. 13, no. 4, 956, **DOI:10.3390/ma13040956**.

[8] Sahu, S., Mohanty, R.C., Panda, R.R., Mohanty, A.M., Arka, G.N. (2018). Optimization of EDM Machining Parameters to Machine INCONEL - 825. *International Journal of Engineering and Management Research*, vol. 8, no. 02, **DOI:10.31033/ijemr.v8i02.11786**.

[9] Shi, W.T., Liu, Y.D., Ding, Y., Han, B.A. (2011). Manufacture of micro gear shaft based on micro hobbing technology. *Applied Mechanics and Materials*, vol. 55-57, p. 494-497, **DOI:10.4028/www.scientific.net/AMM.55-57.494**.

[10] Şentürk, B., Fetvacı, M. (2024). A modified approach to the rack generation of beveloid gears. *Strojniški vestnik - Journal of Mechanical Engineering*, vol.70, no. 1-2, p. 80-91, **DOI:10.5545/sv-jme.2023.722**.

[11] Tan, R., Chen, B., Peng, C., Li, X. (2015). Study on spatial curve meshing and its application for logarithmic spiral bevel gears. *Mechanism and Machine Theory*, vol. 86, p. 172-190, **DOI:10.1016/j.mechmachtheory.2014.11.023**.

[12] An, L., Zhang, L., Qin, S., Lan, G., Chen, B. (2021). Mathematical design and computerized analysis of spiral bevel gears based on geometric elements. *Mechanism and Machine Theory*, vol. 156, 104131, **DOI:10.1016/j.mechmachtheory.2020.104131**.

[13] Chen, Y., Yao, L. (2018). Study on a method of CNC form milling for the concave convex arc line gear. *The International Journal of Advanced Manufacturing Technology*, vol. 99, p. 2327-2339, **DOI:10.1007/s00170-018-2566-9**.

[14] Chen, Y., Lin, Y. (2021). A calculation method for friction coefficient and meshing efficiency of plastic line gear pair under dry friction conditions. *Friction*, vol. 9, no. 6, p. 1420-1435, **DOI:10.1007/s40544-020-0424-x**.

[15] Chen, Y., Li, Z., Xie, X., Lyu, Y. (2018). Design methodology for coplanar axes line gear with controllable sliding rate. *Strojniški vestnik - Journal of Mechanical Engineering*, vol. 64, no. 6, p. 362-372, **DOI:10.5545/sv-jme.2017.5110**.

[16] Chen, Y., Hu, Y., Lyu, Y., He, G. (2020). Development of a form milling method for line gear: principle, CNC machine, cutter, and testing. *The International Journal of Advanced Manufacturing Technology*, vol. 107, p. 1399-1409, **DOI:10.1007/s00170-019-04771-2**.

[17] Xiao, X., Chen, Y., Ye, C., Zhang, D. (2022). Study on face-milling roughing method for line gears-Design, manufacture, and measurement. *Mechanism and Machine Theory*, vol. 170, 104684, **DOI:10.1016/j.mechmachtheory.2021.104684**.

[18] Chen, Y., Xiao, X. (2021). Sweeping modeling method and contact stress optimization of miniature line gear. International Conference on Mechanical Design. Singapore: Springer Nature Singapore, p. 1313-1327, **DOI:10.1007/978-981-16-7381-8_81**.

[19] Chen, Y., Ding, J., Lv, Y. (2015). Geometric constraints and interference-proof conditions of helix-curve meshing-wheel mechanism. *Transactions of the Canadian Society for Mechanical Engineering*, vol. 39, no. 1, p. 13-28, **DOI:10.1139/tcsme-2015-0002**.

[20] Lyu, Y., Chen, Y. (2019). The maximum contact stress of line teeth of parallel axis line gear. Proceedings of the 5th International *Conference on Mechatronics and Robotics Engineering*, p. 16-22, **DOI:10.1145/3314493.3314524**.

[21] De Vaujany, J.-P., Guingand, M., Remond, D., Icard, Y. (2007). Numerical and experimental study of the loaded transmission error of a spiral bevel gear. *Journal of Mechanical Design*, vol. 129, no. 2, p.195-200, **DOI:10.1115/1.2406089**.

[22] Zhang, D.-W., Zheng, Z.-H., Zhao, S.-D. (2019). Influence of geometric parameters on variation of motion during rolling process of involute spline. *Journal of the Brazilian Society of Mechanical Sciences and Engineering*, vol. 41, 208, **DOI:10.1007/s40430-019-1710-2**.

[23] Na, R., Jia, K., Miao, S., Zhang, W., & Zhang, Q. (2023). Analysis of the Dynamic Characteristics of a Gear-Rotor-Bearing System with External Excitation. *Strojniški vestnik - Journal of Mechanical Engineering*, vol. 69, no. 1-2, p. 17-31, **DOI:10.5545/sv-jme.2022.427**.

[24] Wang, C.Y. (2012). Design of planetary gear reducer with double circular-arc helical gear. Applied Mechanics and Materials, vol. 152-154, p. 1595-1600, **DOI:10.4028/www.scientific.net/AMM.152-154.1595**.